

Characteristics of Pristine Thin-Film Transistors

Introduction

Several different approaches were followed to fabricate carbon nanotube network and graphene field-effect transistors for biosensor use. The three carbon nanotube film types used for devices were the solvent-deposited, surfactant-deposited and steam-assisted surfactant-deposited (steam-deposited) films discussed in ?@sec-fabrication. As minor changes were made to fabrication processes throughout the thesis, the fabrication dates of devices used are stated, alongside a brief description of the process used at the time. This chapter looks to use the characterisation techniques outlined in ?@sec-fabrication to compare and contrast the device channel morphologies and electrical characteristics resulting from the various methods used. The other aim of this chapter is to show the electrical behaviour of the transistors when exposed to vapour in the vapour delivery system discussed in ?@sec-vapour-sensing-biosensors.

Atomic force microscopy and Raman spectroscopy were performed on the carbon nanotube networks to identify the distribution of carbon nanotube diameters and the extent to which defects were present on the carbon nanotube networks. Electrical characterisation was then used to see how the morphology of each film type affected the performance of the completed devices. Both back-gated and liquid-gated transfer characteristics were compared, and figures of merit from the liquid-gated characteristics were examined. Control measurements were also taken to verify the behaviour of the pristine device as a sensor in both liquid-gated and vapour-phase environments. In the liquid-phase, a salt concentration sensing series was performed with a steam-deposited carbon nanotube network device. The device characteristics were taken and device drift was examined and modelled. The sensing series was performed by successively diluting 1× PBS in the polydimethylsiloxane ‘well’ (electrolyte container) while passing a current through the device, and measuring the current response to dilutions. Various filters were applied to the collected data to better understand the signal change. Finally, device responses to ethyl hexanoate and *trans*-2-hexanal in a vapour-phase environment were measured and compared to that of off-the-shelf reference sensors.

Carbon Nanotube Network Morphology and Composition

Atomic Force Microscopy

Figure 1 shows a side-by-side comparison of the surface morphology of carbon nanotube films fabricated using the methods described in ?@sec-dep-carbon-nanotubes. These images were collected using an atomic force microscope and processed in the manner described in ?@sec-afm-characterisation. As discussed in previous works using solvent-based deposition techniques for depositing carbon nanotubes, in each network multi-tube bundles form due to strong mutual attraction between nanotubes [@Zheng2017; @Murugathas2018; @Murugathas2019; @Nguyen2021]. However, when surfactants are present, they adsorb onto

the carbon nanotubes and form a highly repulsive structure able to overcome the strong attraction between nanotubes. This repulsion keeps the individual carbon nanotubes relatively isolated [@Wenseleers2004; @Gavrel2013; @Hermanson2013-16; @Shimizu2013; @Di-Crescenzo2014; @Yang2023]. The diameter range provided by the supplier for the individual carbon nanotubes used is 1.2–1.7 nm, while the length range is 0.3–5.0 μm (Nanointegrис).

It has previously been demonstrated that the diameter range of deposited single-walled carbon nanotubes can be modelled via a normal or Gaussian distribution [@LeMieux2008; @Liu2013; @Vobornik2023]. However, when the height profiles from the 2.5 $\mu\text{m} \times 2.5 \mu\text{m}$ AFM images are directly extracted and binned, as shown in Figure 1, the histograms obtained do not follow a normal distribution. One reason for this result is that the carbon nanotubes do not lie perfectly flat on the substrate surface, as the SiO_2 substrate and the carbon nanotubes each possess some surface roughness. To find the contribution of substrate surface roughness to the height profile histogram corresponding to each network deposition method, SiO_2 substrates were modified using the same processes as in Figure 1 but without carbon nanotubes present in the solutions used. 2.5 $\mu\text{m} \times 2.5 \mu\text{m}$ AFM images of the modified surfaces are shown in Figure 2.

In Figure 2, it appears that each substrate surface has a roughness that follows a normal distribution with some degree of skewness. Figure 2 (b) and Figure 2 (d) are negatively skewed distributions. The equation for a skew-normal distribution is given in Equation 1.

$$f(x) = 2\phi(x)\Phi(\alpha x) \quad (1)$$

Within Equation 1, α is the ‘slant parameter’ which indicates the skewness of the distribution, $\phi(x)$ is the standard normal distribution and $\Phi(x)$ is the corresponding cumulative distribution function. In the most general case, Equation 1 can be modified with the ‘location parameter’ ξ and ‘scale parameter’ ω . These variables respectively correspond to the mean and standard deviation of the skew-free normal distribution when α is set equal to zero. These parameters are inserted into Equation 1 by setting $x \rightarrow (x - \xi)/\omega$ and replacing the factor 2 with $2/\omega$ [@Azzalini2013]. The fitted skew-normal distribution in Figure 2 (b) has $\alpha = -3.2$, $\xi = 2.2 \text{ nm}$ and $\omega = 0.5 \text{ nm}$, while in Figure 2 (d) $\alpha = -2.2$, $\xi = 2.2 \text{ nm}$ and $\omega = 0.5 \text{ nm}$. The close correspondence of ξ and ω between these distributions implies that the skewness is a variable imaging or processing artifact rather than a physical property of the surface. Without distortion, the roughness of a clean SiO_2 surface should follow a normal distribution [@Velicky2015].

Figure 2 (f) has a pronounced positive skew $\sim 5.5 \text{ nm}$ in length. The tail results from the droplets observed in Figure 2 (e), which may be condensation from the steam or surfactant residue trapped by the steam environment [@Christensen2022; @Vobornik2023]. If the contamination identified here is surfactant, this could have negative effects on both sensitivity of carbon nanotubes and also could damage the attached biological elements. Attempting to fit a skew-normal distribution to this histogram fails when all three variables are allowed to vary, which results from the presence of the tail. Instead, previous values obtained for ξ and ω can

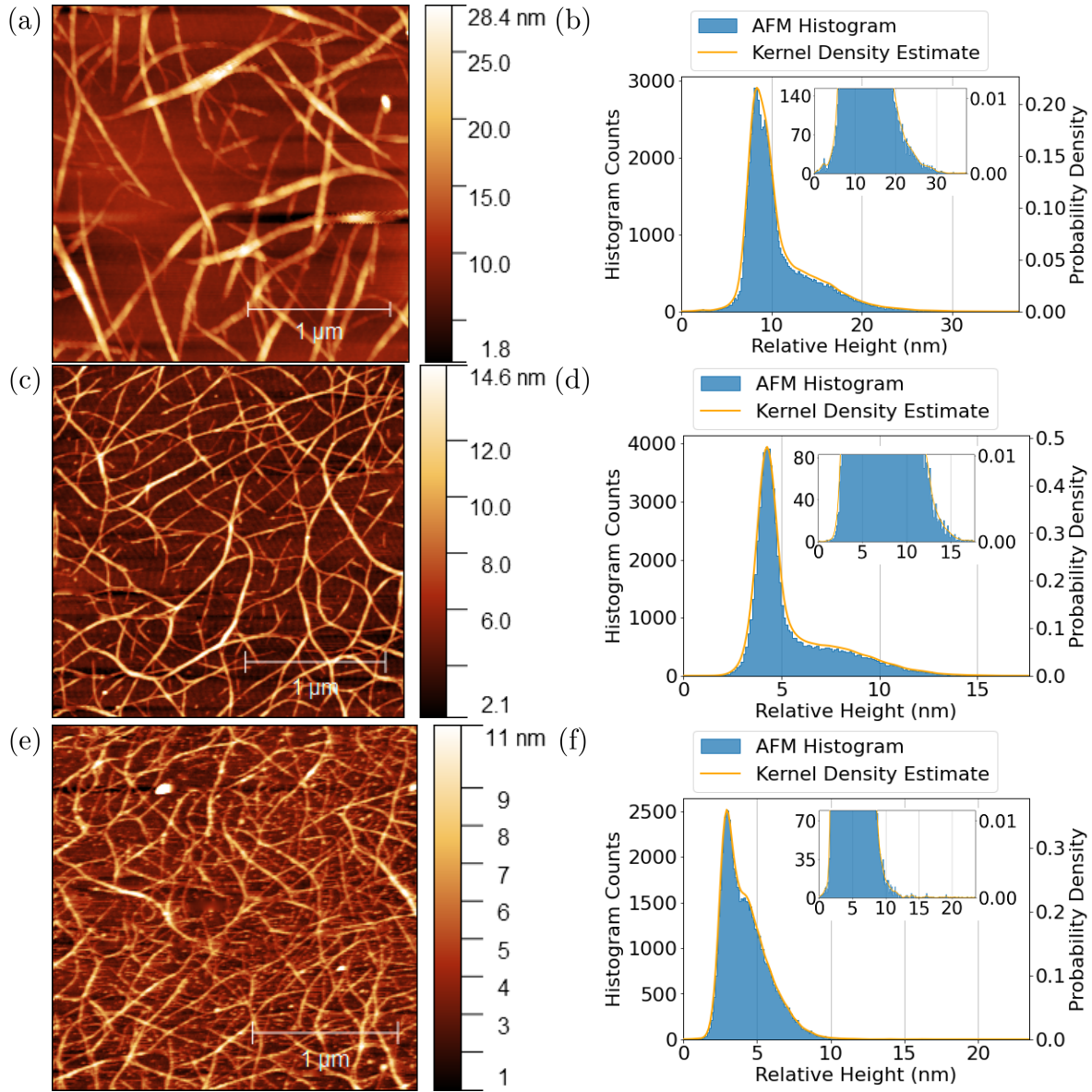


Figure 1: $2.5 \mu\text{m} \times 2.5 \mu\text{m}$ atomic force microscope (AFM) images of carbon nanotube films deposited using various methods, shown side-by-side with histogram height distributions and kernel density estimate (KDE) plots corresponding to each image. The network shown in (a) with height distribution shown in (b) was deposited in solvent, the network shown in (c) with height distribution shown in (d) was dropcast in surfactant, and the network shown in (e) with height distribution shown in (f) was dropcast in surfactant with steam present.

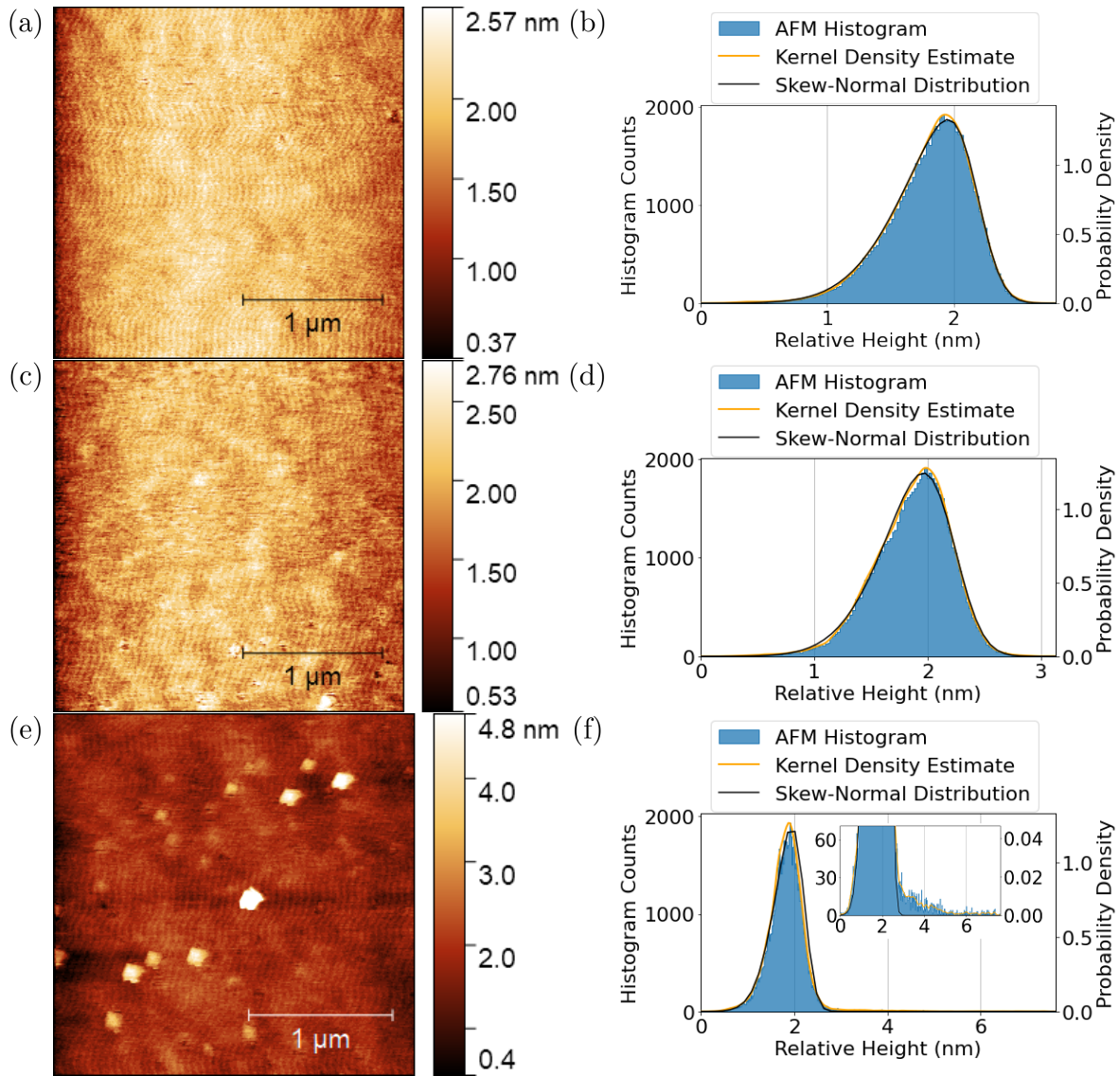


Figure 2: $2.5 \mu\text{m} \times 2.5 \mu\text{m}$ atomic force microscope (AFM) images of SiO_2 substrates alongside histogram height distributions and KDE plots corresponding to each image. The substrate in (a) and (b) was exposed to solvent, the substrate in (c) and (d) was exposed to surfactant, and the substrate in (e) and (f) was exposed to surfactant with steam present. The inset in (f) shows a close-up view of the long tail of the distribution.

be fixed at ξ and ω at 2.2 nm and 0.5 nm respectively in the fitting process, assuming that these values are characteristic of the imaging process used and not the substrate. In this fitting process, therefore, only α was allowed to change. The resulting fitted distribution is shown in Figure 2 (f), with $\alpha = -2.4$. The distribution closely fits the negative tail of the histogram, but deviates from the positive tail due to the presence of the droplets. This deviation is small and the fit is otherwise good quality, with an R-squared value of 0.98.

In the atomic force microscope images of the more highly bundled networks, the carbon nanotube bundles can be distinguished from the substrate background by eye. Therefore, it was reasonably straightforward to use network morphology analysis techniques similar to those previously outlined by Vobornik *et al.* [@Vobornik2023]. In Gwyddion, two coloured height thresholds or ‘masks’ were defined, one which covered all exposed substrate along with small bundles, shown in Figure 3 (a)-(b), and one which covered all substrate but excluded all bundles, shown in Figure 3 (c)-(d). The median substrate height across both substrate masks was 8.4 ± 0.5 nm for the solvent-deposited film, and 4.3 ± 0.1 nm for the surfactant-deposited film, where the medians of the individual masks for each film were used to give the upper and lower bounds of uncertainty. These values are dramatically different from the median substrate height of 1.9 ± 0.3 nm obtained from the distributions in Figure 2. From comparing the atomic force microscope images in Figure 2 with Figure 3, it does not appear a dramatic increase in substrate surface roughness has occurred after carbon nanotube deposition. Instead, it appears that the discrepancy between these values results from the imaging process.

In Figure 1, deep streaks or scars with rounded edges can often be found in the close vicinity of larger nanotube bundles and junctions. These features appear to be imaging artifacts, which sometimes sit at heights well below the actual substrate surface. The artifacts result from the microscope tip taking inaccurate surface measurements when moving from scanning a large feature to scanning a much smaller one [@Ukrainstsev2012]. Imaging artifacts are highlighted using a mask in Figure 3 (e)-(f), with heights of 6.4 ± 0.4 nm and 2.7 ± 0.2 nm for the solvent-deposited and surfactant-deposited films respectively. By adding the median substrate height from Figure 2 to the artifact heights, average background values of 8.3 ± 0.7 nm and 4.6 ± 0.5 nm are obtained for each film, both within error of the median substrate heights obtained using Figure 3. It can be stated with confidence that the median value obtained from the substrate mask is representative of the actual average substrate level relative to the carbon nanotubes present, unaffected by image artifact outliers. These median values can be used to compare the height of carbon nanotube bundles to the average height of the surrounding substrate, following the same approach as Vobornik *et al.* [@Vobornik2023].

Five successive diameter measurements of 30 carbon nanotube bundles distributed evenly across the network were collected using Gwyddion. Measurements were not taken at bundle junctions. The average of five values for each carbon nanotube bundle was then taken and the corresponding background height of the substrate subtracted. The 30 height values were sorted into five equal-sized bins, as shown in Figure 4. Each histogram appears to follow a moderately positive-skewed normal distribution, different to the skew-free normal distribution found in previous works [@LeMieux2008; @Liu2013; @Vobornik2023]. The skew therefore

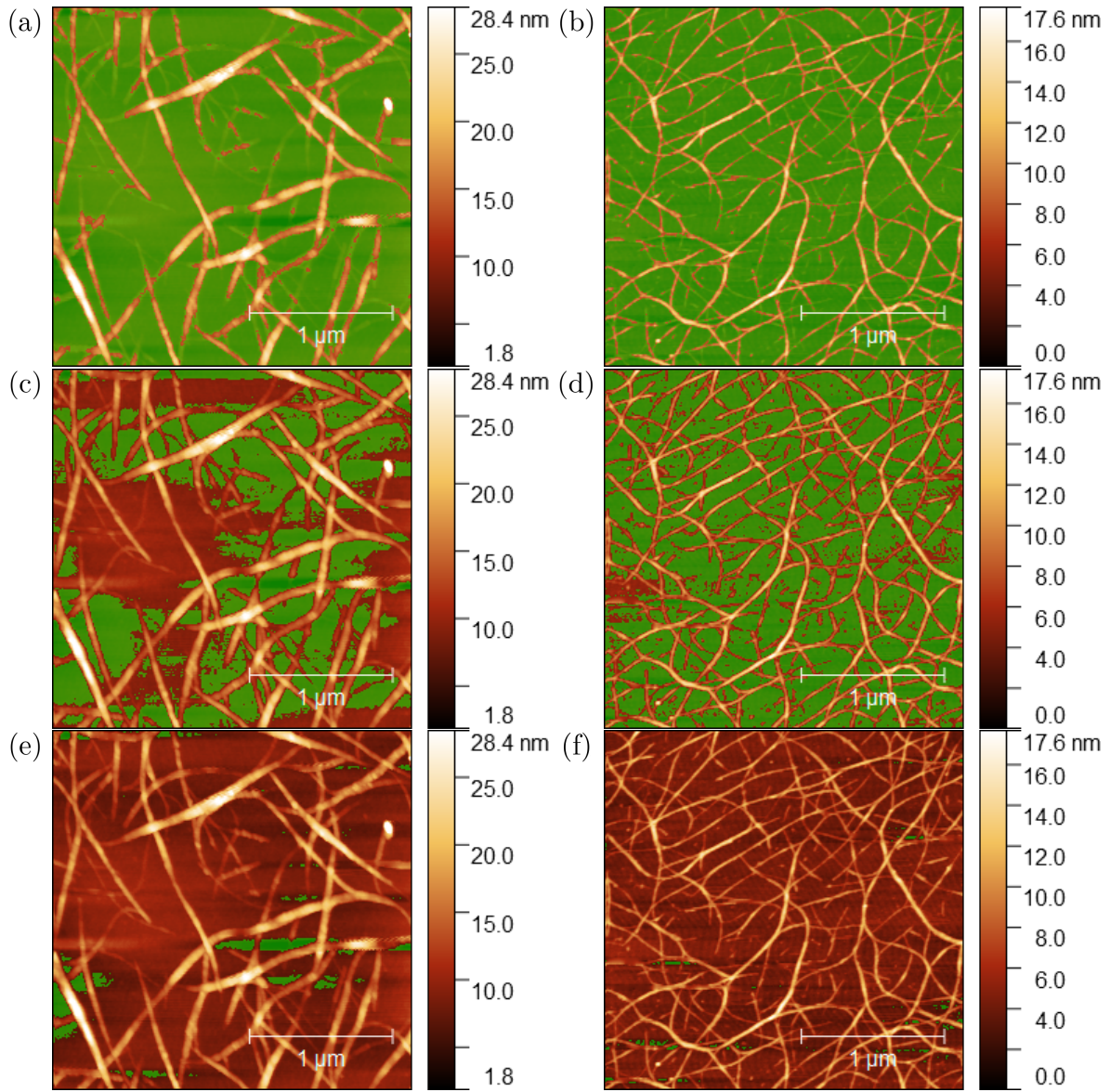


Figure 3: A mask, shaded green, sets a height threshold so that masked features are hidden from the height dataset. The network in (a), (c) and (e) was solvent-deposited, while the network in (b), (d) and (f) was surfactant-deposited. The maximum possible substrate height of each network is masked in (a) and (b), the maximum possible substrate height excluding all carbon nanotubes is masked in (c) and (d), while artifacts below the substrate surface have been masked in (e) and (f).

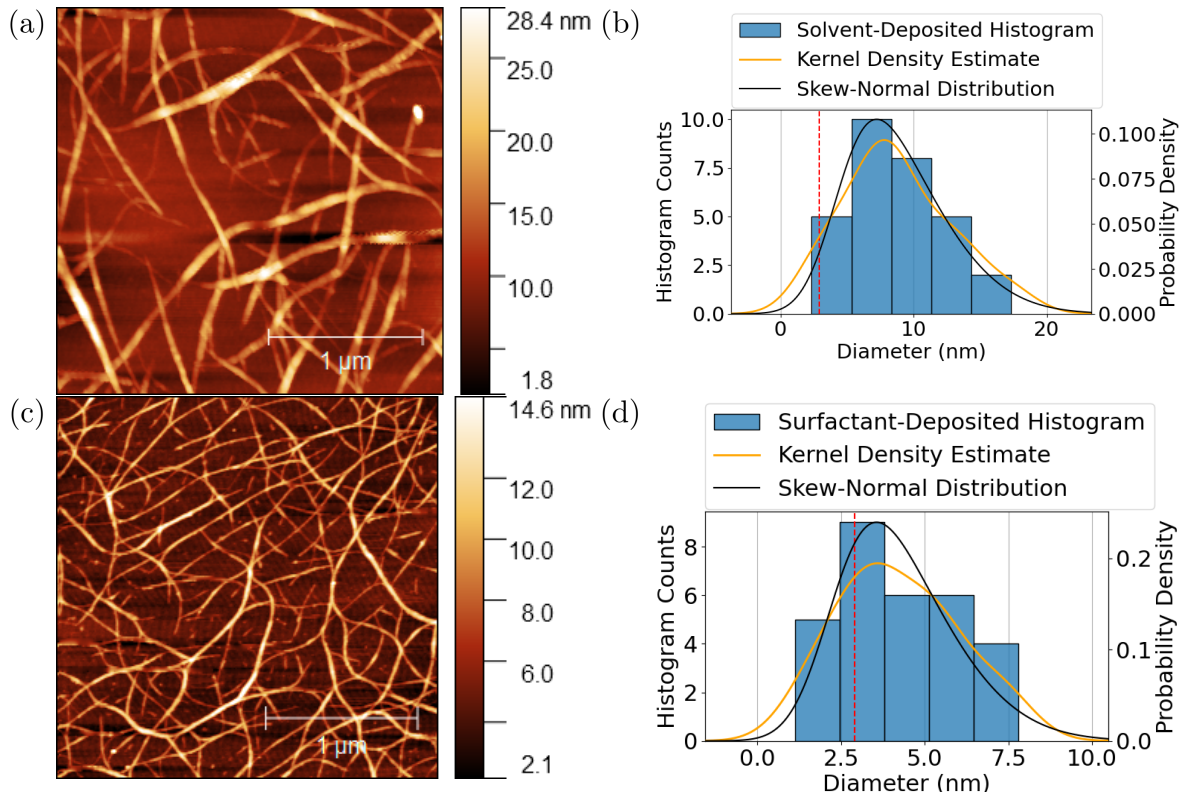


Figure 4: Histogram height distributions for each carbon nanotube network with corresponding kernel density estimate plots collected via the morphology analysis method outlined by Vobornik *et al.* [Vobornik2023]. The histogram for the solvent-deposited network in (a) is shown in (b) and the histogram for the surfactant-deposited network in (c) is shown in (d). The red dotted line represents the lower bound for multi-tube bundles at 2.9 nm, assuming the minimum nanotube diameter is 1.45 nm.

appears to be a distortion, introduced by the imaging process. The force of the atomic force microscope tip is known to cause larger bundles to undergo some degree of compression, and the resulting systematic underestimation of their height may be responsible for the distribution skewness [@Vobornik2023]. The fitted skew-normal distribution in Figure 4 (b) has $\alpha = 2.7$ (slant, indicates skew), $\xi = 4.3$ nm (location, indicates mean), and $\omega = 5.9$ nm (scale, indicates standard deviation), while the distribution in Figure 4 (d) has $\alpha = 2.5$, $\xi = 2.2$ nm, and $\omega = 2.6$ nm. The probability density for the carbon nanotube bundle histogram drops to approximately zero at 0 nm, an indication that the dataset is representative of the actual film.

```
#|  
  
knitr::opts_chunk$set(echo = FALSE)  
library(knitr)  
library(kableExtra)  
  
circle_packing <- read.csv("tables/ch5/circle_packing.csv", sep=",")  
circle_packing <- circle_packing[rowSums(is.na(circle_packing)) == 0,]  
  
knitr::kable(circle_packing, col.names = NULL, format = "simple")
```

Table 1: The first eight optimised ratios of 2D packed circle diameter to encompassing circle diameter, given to 3 s.f. (encompassing circle diameter = d , number of packed circles = n , approximate packed circle diameter = d_n).

n	2	3	4	5	6	7	8	9
d/d_n	2.00	2.15	2.41	2.70	3.00	3.00	3.30	3.61

Analysis of carbon nanotube network morphology can be simplified by assuming the component nanotubes are cylinders, follow 2D packing and are of equal diameter [@Murugathas2018]. Table 1 shows the relationship between the diameter of a bundle of 2D packed cylinders and their constituent diameters. Assuming an average carbon nanotube diameter of 1.45 nm, it is possible to use Table 1 to find the approximate number of nanotubes, n , present in the median bundle diameter of a film, where the median bundle diameter is taken from the distributions in Figure 4. An estimate of the relative proportion of multi-tube bundles in a film can be found by taking the integral of each probability distribution with a lower bound of 2.9 nm, the minimum multi-tube bundle size for 1.45 nm diameter nanotubes. Since the area under the curve represents the probability a bundle will have a particular diameter, the ratio of the bounded integral to the unbounded integral gives a reasonable estimate of the proportion of multi-tube bundles relative to single nanotubes. The proportion of substrate covered by nanotubes can be determined by comparing the projected surface area of the masks in Figure 3 (a)-(d) with the full image area.

These estimates are all shown in Table 2, with the caveat that median bundle diameter is likely being underestimated due to tip compression [@Vobornik2023]. Alternative estimates for median bundle diameter can be obtained by finding the median heights of the combined unmasked regions from Figure 3 (a) and (c) and from Figure 3 (b) and (d), which are 12.7 ± 2.6 nm and 8.0 ± 0.9 nm respectively. By subtracting the median substrate height of each image, 8.4 ± 0.5 nm and 4.3 ± 0.1 nm, alternative median bundle diameters of 4.3 ± 3.1 nm and 3.7 ± 1.0 nm are found, within the error margin of the values in Table 2. Both the carbon nanotube bundle diameter median and standard deviation are small for surfactant-deposited films when compared to the median and standard deviation of solvent-deposited films. However, despite the presence of surfactant, it is apparent both from Figure 4 and Table 2 that most surfactant-dispersed carbon nanotubes are not deposited individually. It is possible that the bundling of surfactant-dispersed carbon nanotubes occurs as nanotubes are deposited onto the surface, as this bonding process may disrupt the repulsive forces from the surfactant coating and allow attractive forces to temporarily dominate.

Table 2: The median of histogram distributions for solvent-deposited and surfactant-deposited carbon nanotube films, alongside rough estimates for the number of nanotubes present per median bundle, the estimated proportion of multi-tube bundles present across the network and the proportion of substrate covered by the nanotubes.

	Median Bundle Diameter (nm)	Tubes per Median Bundle	% Multi-Tube Bundles	% Nanotube Coverage
Solvent-deposited	8.3 ± 4.5	24	> 97%	< 66%
Surfactant-deposited	3.9 ± 1.9	4	> 77%	< 40%

* Dense Nanotube Networks

The solvent-deposited and surfactant-deposited networks in Figure 1 (a)-(d) are relatively sparse, while the steam-deposited film seen in Figure 1 (e)-(f) shows a dense network of single and less-bundled nanotubes, along with some larger bundles. It was unclear whether the method of Vobornik *et al.* could be used due to difficulty distinguishing small nanotubes from the substrate, but a similar approach was attempted. The dual-masking technique seen earlier was used to estimate the substrate height. The first mask covers all exposed substrate, including small bundles, as shown in Figure 5 (a). The second mask is set empty, assuming that almost the entire surface is densely covered with carbon nanotubes. The median height of the masked region is 2.2 ± 0.3 nm. Artifact regions with a height of 0.7 ± 0.2 nm are highlighted in the top-left corner of Figure 5 (b). Assuming the actual substrate surface is visible in atomic force microscope image, its height is estimated by adding the artifact height to the median substrate height of 1.9 ± 0.3 nm from Figure 2, which yields 2.6 ± 0.5 nm. This estimate aligns

with the masking result found previously, indicating it gives a reasonable estimate of substrate height even for dense networks.

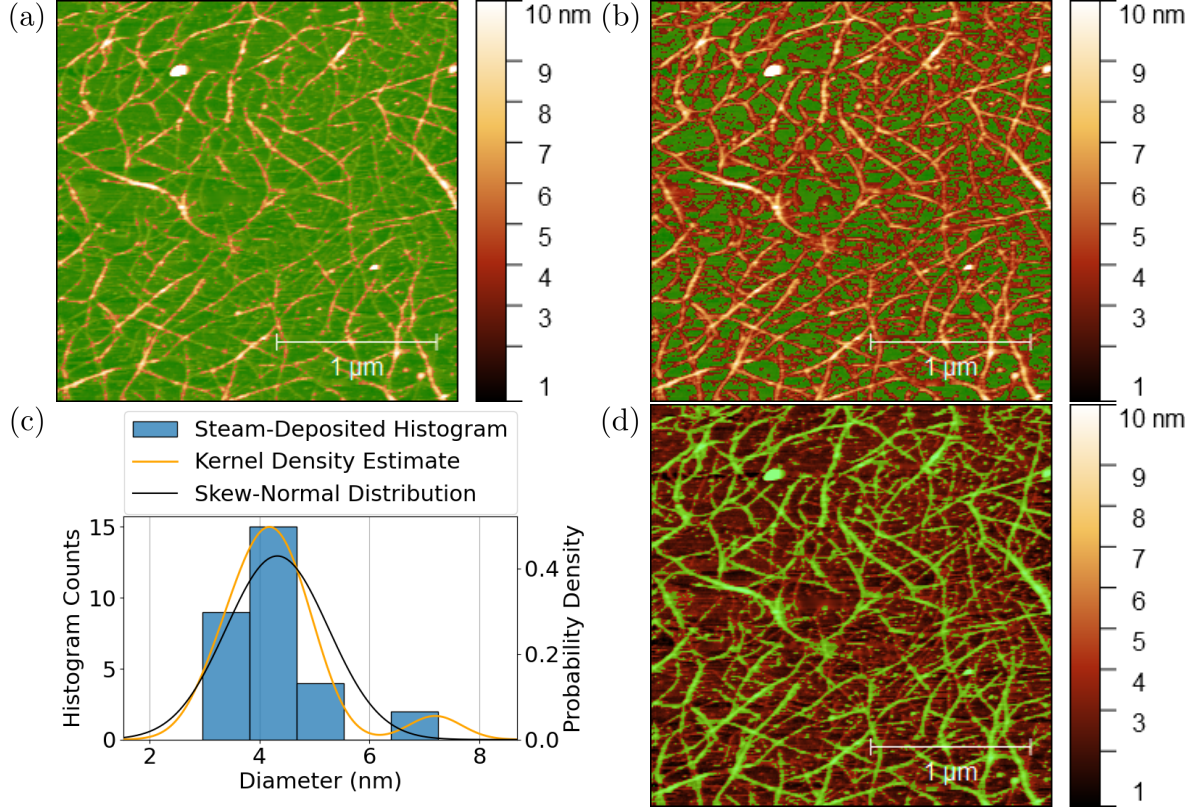


Figure 5: The dense steam-deposited network is covered with a mask showing the maximum possible height of the substrate in (a) and covered with a mask highlighting imaging artifacts in (b). A histogram of bundle measurements above the median substrate height is shown in (c), while a mask covering all regions with height at or greater than the median carbon nanotube diameter is shown in (d).

Taking binned diameter measurements of the larger bundles, as seen earlier, gives the histogram shown in Figure 5 (c). Unlike the skew-normal distributions seen earlier, the distribution in Figure 5 (c) falls to zero at ~ 1 nm. This unphysical result comes from undercounting the large population of smaller nanotubes, which in turn results from less-bundled nanotubes being difficult to distinguish from the substrate background. It is still possible to use masking to obtain an estimate of the median bundle height. The median height of the combined unmasked regions in Figure 5 (a)-(b) is 4.1 ± 0.2 nm, with all regions in the network at or above this height shown in Figure 5 (d). The median substrate height, 2.2 ± 0.3 nm, can be subtracted from the unmasked region height for a median bundle diameter of 1.9 ± 0.5 nm. This estimate is approximately half that of the median bundle diameter in the film deposited with surfactant without steam present. This result implies the presence of steam disrupts the bundling of

carbon nanotubes during deposition. However, it is also possible that no substrate is visible in Figure 5, and the two films have similar bundle sizes once the resulting height offset is taken into account.

The discussion in this section gives us a new understanding of the histograms shown in Figure 1. It appears that these histograms are linear combinations of skewed normal distributions. These distributions include a negatively-skewed distribution corresponding to the substrate surface and a positively-skewed distribution corresponding to the carbon nanotube bundles. The trough-like image artifacts as well as X and Y junctions between overlapping nanotubes may also form similarly skewed normal distributions as part of the complete image histogram [@Murugathas2018]. The linear combination of histograms could be modelled mathematically in order to rapidly extract key parameters from atomic force microscope images [@Marchenko2010], but implementing this approach is outside of the scope of this thesis. Introducing steam when depositing with surfactant visibly promotes even surface coverage, but also leads to increased adsorption of water and possibly surfactant onto the substrate and network. Finding a method of removing the unwanted surfactant or moisture present may be required for robust biosensors [@Kane2014; @Barnett2018].

Raman Spectroscopy

Raman spectroscopy was also used to analyse and compare the deposited carbon nanotube networks. Raman measurements were collected from a solvent-deposited carbon nanotube film and a steam-assisted surfactant-deposited film, both on SiO_2 , in the manner described in ?@sec-raman-characterisation. These spectra were then processed using the Python script mentioned in ?@sec-raman-analysis. For each location, spectra over two wavenumber ranges were collected. A peak corresponding to the bulk Si/SiO_2 substrate, found in the range between 100 cm^{-1} and 650 cm^{-1} , was used as a reference peak for normalisation of spectral intensity [@E2015]; these normalised spectra are shown in Figure 6. In nanotube networks, the properties of individual nanotubes influence the frequency of vibrational modes excited by the inelastic scattering of incident laser light, and therefore the location of peaks in the resulting Raman spectrum. In carbon nanotube network spectra, a D-band comprising a single D-peak is typically observed at $\sim 1320 \text{ cm}^{-1}$, and a G-band comprising two G-peaks, G^- and G^+ , is observed between $\sim 1525 \text{ cm}^{-1}$ and $\sim 1650 \text{ cm}^{-1}$, as seen in Figure 6 (a)-(b) [@Dresselhaus2005; @King2014; @E2015].

Closer inspection of the D-peak and G-peaks in Figure 6 can give us important information about the composition of the nanotube network. G^- is a minor peak found at $\sim 1570 \text{ cm}^{-1}$, while G^+ is a larger feature at $\sim 1590 \text{ cm}^{-1}$. The G^+ feature is associated with semiconducting nanotubes and describes the in-plane vibration of bonds along the nanotube length, while the G^- feature is associated with metallic nanotubes and describes the in-plane vibration of bonds about the nanotube circumference [@King2014; @Swiniarski2021]. The G^+ feature has a sharp Lorentzian lineshape, while the G^- feature has an asymmetric Breit-Wigner-Fano

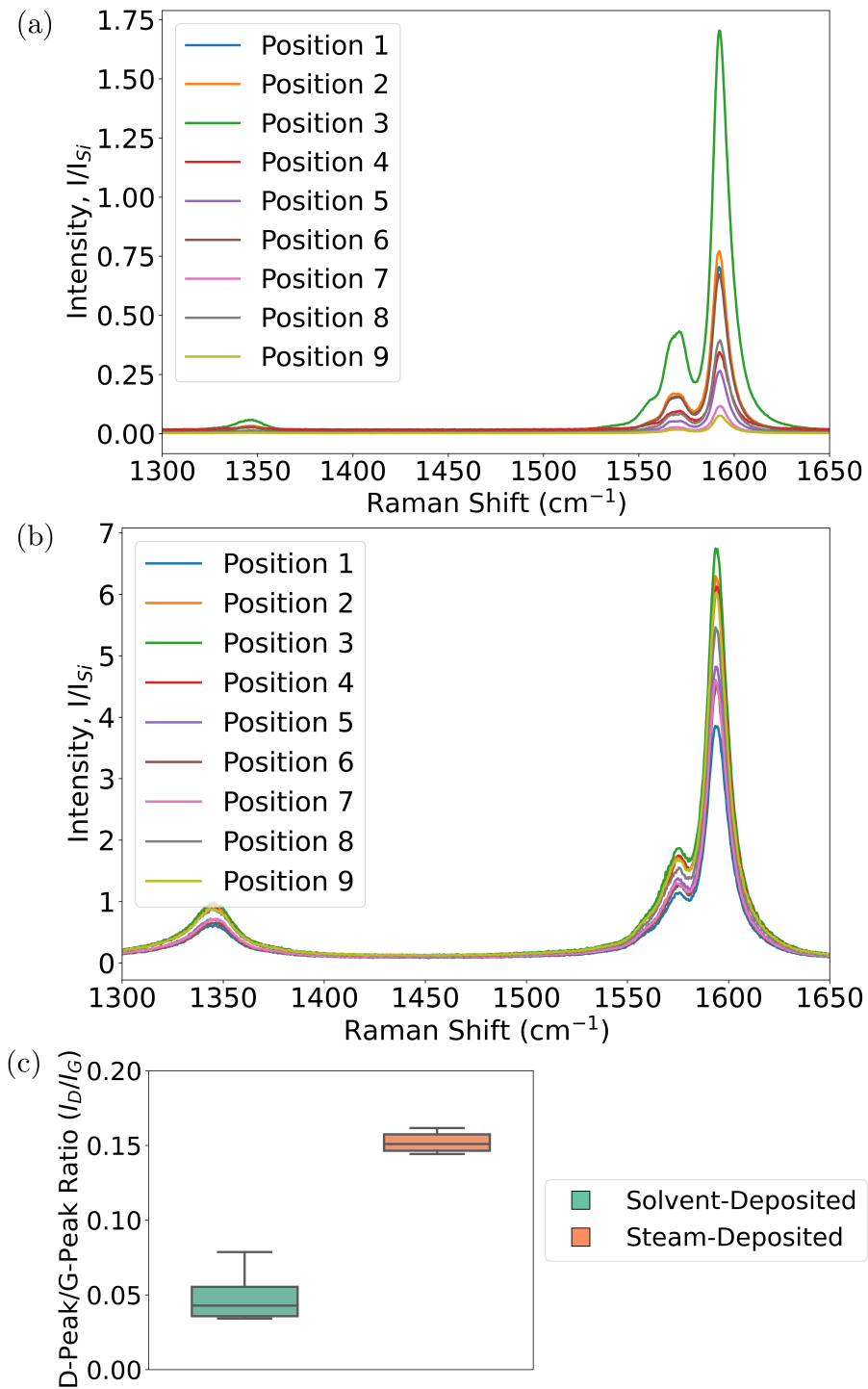


Figure 6: A series of nine Raman spectra at different locations across a $40 \mu\text{m} \times 100 \mu\text{m}$ carbon nanotube film region, where (a) shows spectra from a film deposited using solvent while (b) shows spectra from a film deposited with surfactant in the presence of steam. (c) shows a histogram of the range of D-peak/G⁺-peak spectral ratios corresponding to each film.

(BWF) lineshape [@Blackburn2006; @Swiniarski2021]. The splitting between the wavenumber location of the G⁻ and G⁺ local maxima is lower in Figure 6 (b) than in Figure 6 (a), which may indicate more metallic nanotubes are present in the surfactant-deposited network [@Swiniarski2021]. The D-peak is a ring-breathing mode which indicates defects are present in the carbon nanotube atomic structure; the ring-breathing mode results from the defects disrupting in-plane lattice vibration [@King2014; @CuentasGallegos2011; @Swiniarski2021]. The size of the normalised D-peak appears much smaller in Figure 6 (a) than in Figure 6 (b), indicating the solvent deposition process introduces fewer defects to the carbon nanotubes than surfactant-mediated deposition.

Carbon nanotube structural disorder can be quantified by comparing the relative magnitude of the D-peak and G⁺-peak intensity [@Dresselhaus2005; @King2014]. Figure 6 (c) compares the ratio between D-peak and G⁺-peak intensity across all nine positions across the solvent-deposited and the surfactant-deposited films. The spread of values for the I_D/I_G ratio is lower for the steam-deposited network. This spatially homogeneous vibrational behaviour reflects the steam-deposited film being more evenly distributed, as discussed in Section . It is also observed that I_D/I_G is larger for the steam-deposited films than for the solvent-deposited films, indicating more defects are present in the steam-deposited film. These defects may be charge impurities introduced by adsorbed water or surfactant [@Christensen2022]. The size of the G⁻ feature relative to the G⁺ feature can also be used to detect charge polarisation due to surfactant presence, though since the G⁻ feature is also sensitive to bundle size, it cannot be used for a direct comparison of surfactant presence for the films in Figure 6. However, if the defects are surfactant, the I_{G^-}/I_{G^+} ratio could be useful for comparing films of similar morphology before and after cleaning steps aimed at removing surfactant, with possible cleaning approaches discussed in ?@sec-future-work-fabrication.

Electrical Characteristics of Pristine Devices

Python Analysis

Analysis of electrical measurements was performed using the three Python modules described in ?@sec-field-effect-transistor-analysis. For all three modules, the type of device being analysed (carbon nanotube or graphene) can be set in the config file. The config file can also be used to add annotations to any plot, to set the procedure for normalising a sensing dataset, and the size of the filter window used for the filters described below. In this work, a filter window of 40 datapoints was used.

The first of the three modules is for processing sensing datasets. Types of plots produced include normalised plots, plots with fitted curves, plots with the linear baseline drift removed, plots of signal against analyte addition, ‘despiked’ plots, ‘filtered’ plots and plots with any combination of these modifications. This module uses the `scipy.optimize.curve_fit` function when fitting exponential and linear curves to regions of the sensing data. It then returns .csv spreadsheets containing the results of these analyses, including the standard deviation

for all calculated parameters. For a linear fit $c_1 t + c_2$, the initial estimates used for c_1 and c_2 were straightforward: $c_1 = 1$ and $c_2 = 0$. For an exponential fit $I_0 \exp(-t/\tau) + I_C$, rough approximations were used for the initial parameters: I_C was set as the final current measurement of the region of interest, I_0 was set as the initial current measurement minus I_C , and τ was set as the time where measured current drops to $e^{-1}I_0 + I_C$.

‘Despiked’ plots had spurious datapoints removed through the use of an interquartile range rolling filter. Datapoints in each window with a z -score above ± 3 were removed from the plotted/processed data. ‘Filtered’ plots had noise reduced using a moving median filter. The moving median filter is more effective at removing noise than a simple moving average. It also has advantages over other filters, such as the Savitzky-Golay or Butterworth filters, when removing noise from data with sharp edges, which is the case for sensing data. Median filtering can also be used for baseline drift compensation, though this approach was not used in this thesis [Stone2011]. A simple difference calculation between the mean of the filtered current before an addition and the mean of the filtered current after the addition was performed at each addition for plots of signal against analyte addition, with examples in Figure 7. This process gave reasonably consistent results between the case where baseline drift was removed, as shown in Figure 7 (a), or not, as shown in Figure 7 (b). This method of calculating signal is therefore robust even when significant drift is present.

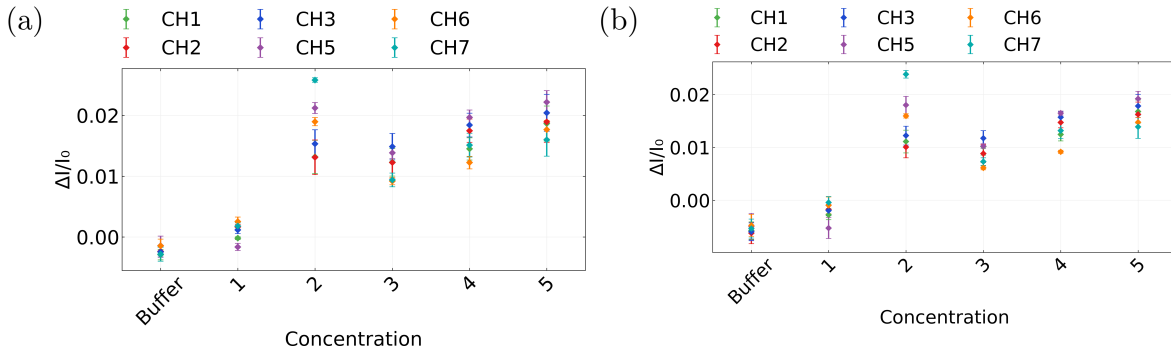


Figure 7: A comparison of signal with analyte addition plots taken from a PBS dilution sensing dataset. In (a), a simple difference before and after addition calculation was performed on filtered data with the baseline drift removed, while in (b), baseline drift was not removed before performing the calculation.

The second module creates combined and individual plots of transfer data collected from eight channels on a single device. In combined plots, shorted or non-conducting channels are removed via setting a maximum and minimum possible on-current in the config file. Various parameters from the transfer characteristics are saved as a spreadsheet along with standard error. These parameters include on current, off current, subthreshold slope and threshold voltage for the carbon nanotube devices, and on current, off current and major Dirac point voltage for graphene devices. The third module allows for comparison of transfer measurements taken of the same channel before and after some modification. It also calculates the shift in

either threshold voltage or major Dirac voltage of the device.

Graphene Devices

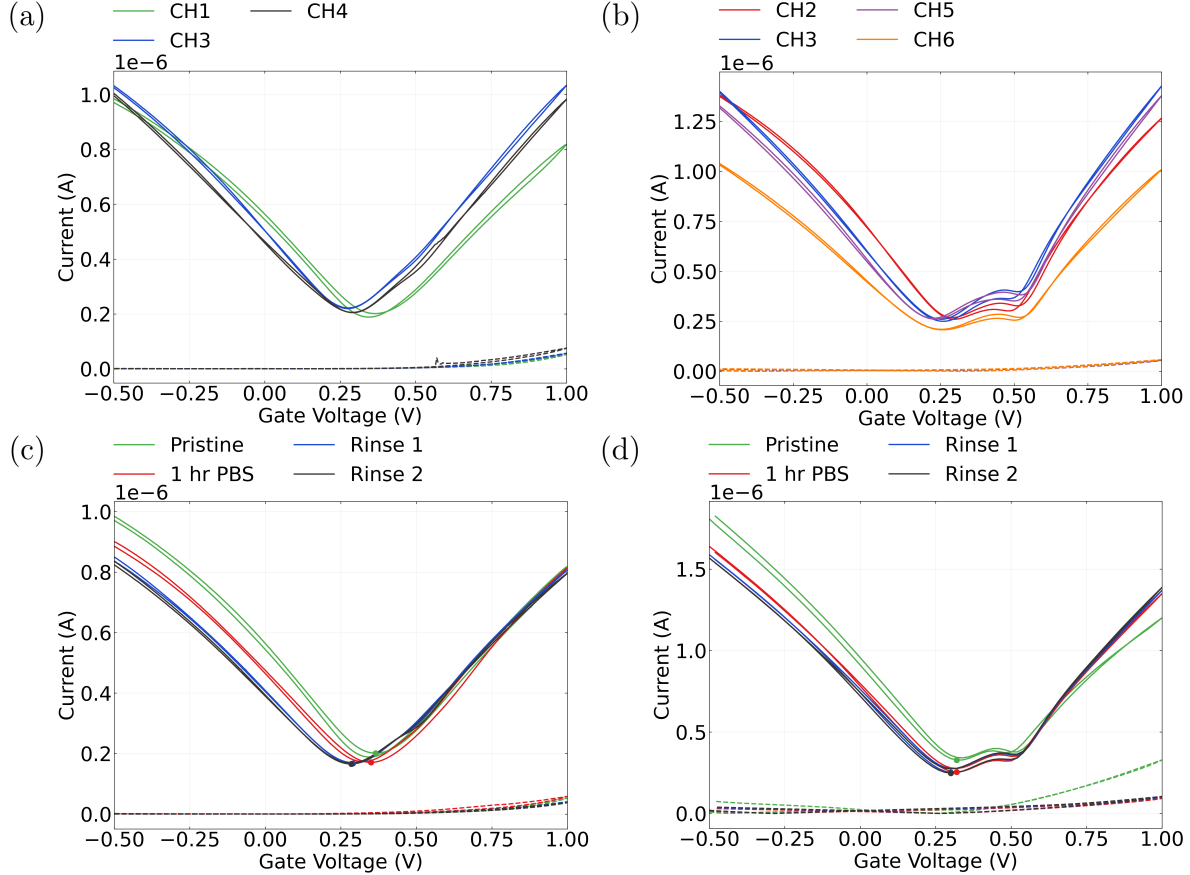


Figure 8: Figures (a) and (b) show liquid-gated transfer characteristics of channels from two AZ® 1518 encapsulated graphene devices. The transfer characteristics of channel 1 in (a) and channel 5 in (b) after various degrees of exposure to 1× PBS are shown in (c) and (d) respectively, with each transfer sweep numbered in the order the sweeps were taken. The dashed lines correspond to measurements of gate leakage current.

Graphene field-effect transistor devices were electrically characterised in the manner described in [?@sec-electrical-characterisation](#) and analysed using the Python code discussed in [?@sec-field-effect-transistor-analysis](#). Figure 8 (a) and (b) show the liquid-gated transfer characteristics of two graphene devices. These devices were fabricated prior to Jun 2021. Both devices exhibit the ambipolar characteristics typical of liquid-gated graphene devices [[@Heller2009a](#); [@Heller2010](#); [@Xia2010](#); [@Kireev2017](#)]. As with the carbon nanotube network devices, leakage current remained below $\sim 1 \times 10^{-7}$ V across both the forward and reverse

sweep. Hysteresis between the forward and reverse sweep is caused by trapping of charge within and on the surface of the SiO_2 dielectric [Bartolomeo2011]. In this work, the global minimum of the transfer characteristic is referred to as the ‘major’ Dirac point while the second Dirac point is referred to as the ‘minor’ Dirac point. The major Dirac point for these devices is slightly to the right of $V = 0$ V, which indicates *p*-doping of the channel. This slight *p*-doping is a result of adsorption of oxygen and water from the air or from residual photoresist [Cheng2011; Shin2012; Kireev2017]. Some devices exhibited double Dirac point behaviour, as seen in Figure 8 (b).

Figure 8 (c) and (d) show the effect of 1× PBS on the graphene channels. The channels were measured on exposure to 1× PBS, after exposure to 1× PBS for one hour, and after two successive rinse steps. A slight negative shift of the major Dirac point was observed. This effect is possibly a result of gate bias stress, where successive transfer sweeps introduce charge traps to the graphene layer and alter the current level at a given gate voltage [Bargaoui2018; Noyce2019]. This effect may also be due to the removal of *p*-doped contamination after rinsing, such as adsorbed oxygen or resist residue, causing interfacial charge traps to empty and resulting in a negative shift of the major Dirac point [Bartolomeo2011; Kireev2017; Peng2018]. Table 3 shows the on-off ratio and major Dirac point voltage of the graphene devices after each modification. Apart from the previously-mentioned slight negative shift of the major Dirac point, these values were highly consistent before and after exposure to 1× PBS.

Table 3: Average on-off ratio and major Dirac point voltage for AZ® 1518 encapsulated liquid-gated graphene transistor channels at various stages of exposure to 1× PBS. Electrical characteristics were taken of 6 channels total, three channels from each of two devices.

	1X PBS: Initial	1X PBS: After 1 hr	1X PBS: Rinse
On-Off Ratio (arb.)	5.1 ± 0.3	5.0 ± 0.7	5.0 ± 0.6
Dirac Point Voltage (V)	0.28 ± 0.04	0.31 ± 0.03	0.28 ± 0.02

Carbon Nanotube Network Devices

Each carbon nanotube device fabricated was electrically characterised as described in ?@sec-electrical-characterisation, and electrical data was analysed using the Python code discussed in ?@sec-field-effect-transistor-analysis. Devices with a 100 nm or 300 nm SiO_2 layer were used for liquid gated measurements, and devices with a 100 nm SiO_2 layer were used for backgated measurements. Figure 9 displays multi-channel measurements of representative devices fabricated as described in ?@sec-fabrication. To ensure a consistent comparison, all device measurements shown here are from devices fabricated and encapsulated using only AZ® 1518 photoresist. The channels which did not exhibit reliable transistor characteristics are not shown. These ‘non-working’ channels were either shorted, due to metal remaining on

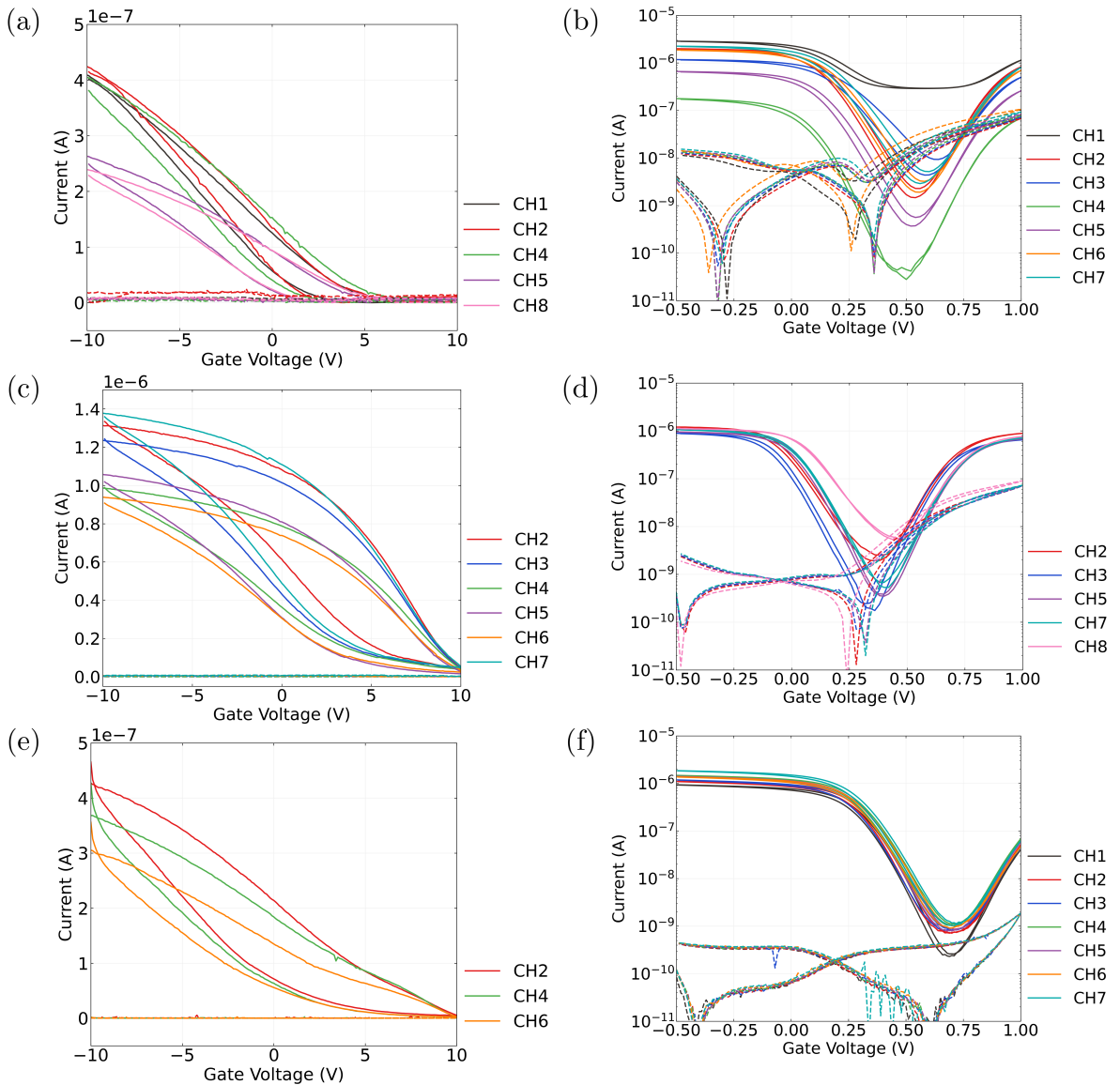


Figure 9: Back-gated (left) and liquid-gated (right) transfer characteristics of AZ® 1518 encapsulated field-effect transistors, where the film was deposited with solvent in (a) and (b), deposited with surfactant in (c) and (d), and deposited with surfactant in the presence of steam in (e) and (f). A step size of 100 mV was used for the backgated sweeps in (a), (c) and (e), while a step size of 20 mV was used for the liquid-gated sweeps in (b), (d) and (f). Gate current (leakage current) is shown with a dashed line. The source-drain voltage used for all sweeps was $V_{ds} = 100\text{mV}$, and 1× PBS was used as the buffer for the liquid-gated measurements here.

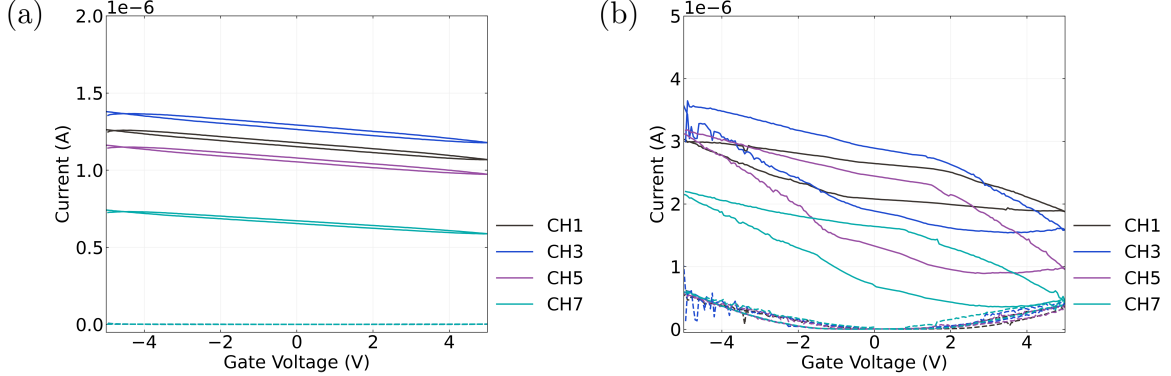


Figure 10: Backgated transfer sweeps were taken of an single unencapsulated device with a 300 nm SiO_2 layer and steam assisted surfactant-deposited carbon nanotube network channels before and after being covered in 50 μL 1 \times PBS.

the channel after lift-off, or were very low current, due to a very sparse carbon nanotube network. Devices shown here with a solvent-deposited carbon nanotube network were fabricated prior to Jan 2022; devices with a surfactant-deposited network without steam present were fabricated prior to Jun 2021; devices with a surfactant-deposited network without steam were fabricated prior to Sep 2022.

When characterising devices using the vapour delivery system chip carrier, the setup arrangement meant all measurements were taken using a backgate. Figure 9 (a), Figure 9 (c) and Figure 9 (e) show that backgated devices exhibit *p*-type transistor behaviour. Gate current leakage was negligible, as shown by the dashed line staying close to zero across the sweep. The hysteresis observed was much greater than for the corresponding liquid-gated sweeps on the left. This hysteresis can be explained by the presence of defects or charge traps within and on the surface of the gate-insulating SiO_2 and at interfaces between SiO_2 and carbon nanotubes. The occupancy of these charge traps evolves over time with applied gate voltage [@Lee2007; @Lee2012; @Ha2014]. The devices fabricated with a solvent-based deposition had a significantly lower off-current than the surfactant-deposited devices, which may result from very few metallic nanotubes being present in the less-dense network [@Rouhi2011] used to create the device with characteristics shown in Figure 9 (a).

Transfer measurements were taken to determine whether backgated measurements could be taken of an unencapsulated device in the vapour sensor chamber with 1 \times PBS covering the channels. The use of a backgated configuration with channels in a liquid environment is generally considered less than ideal, since the sensitivity of the device is greatly reduced [@Li2023]. Figure 10 and (b) show the behaviour of an unencapsulated backgated device before and after being covered by 50 μL of 1 \times PBS. The on-off ratio and hysteresis of the channels both increase significantly. The presence of water increases hysteresis through introducing charge traps at the SiO_2 surface around the carbon nanotubes and at the surface of the nanotubes themselves [@Kim2003; @Lee2007; @Franklin2012; @Ha2014]. There is also a significant in-

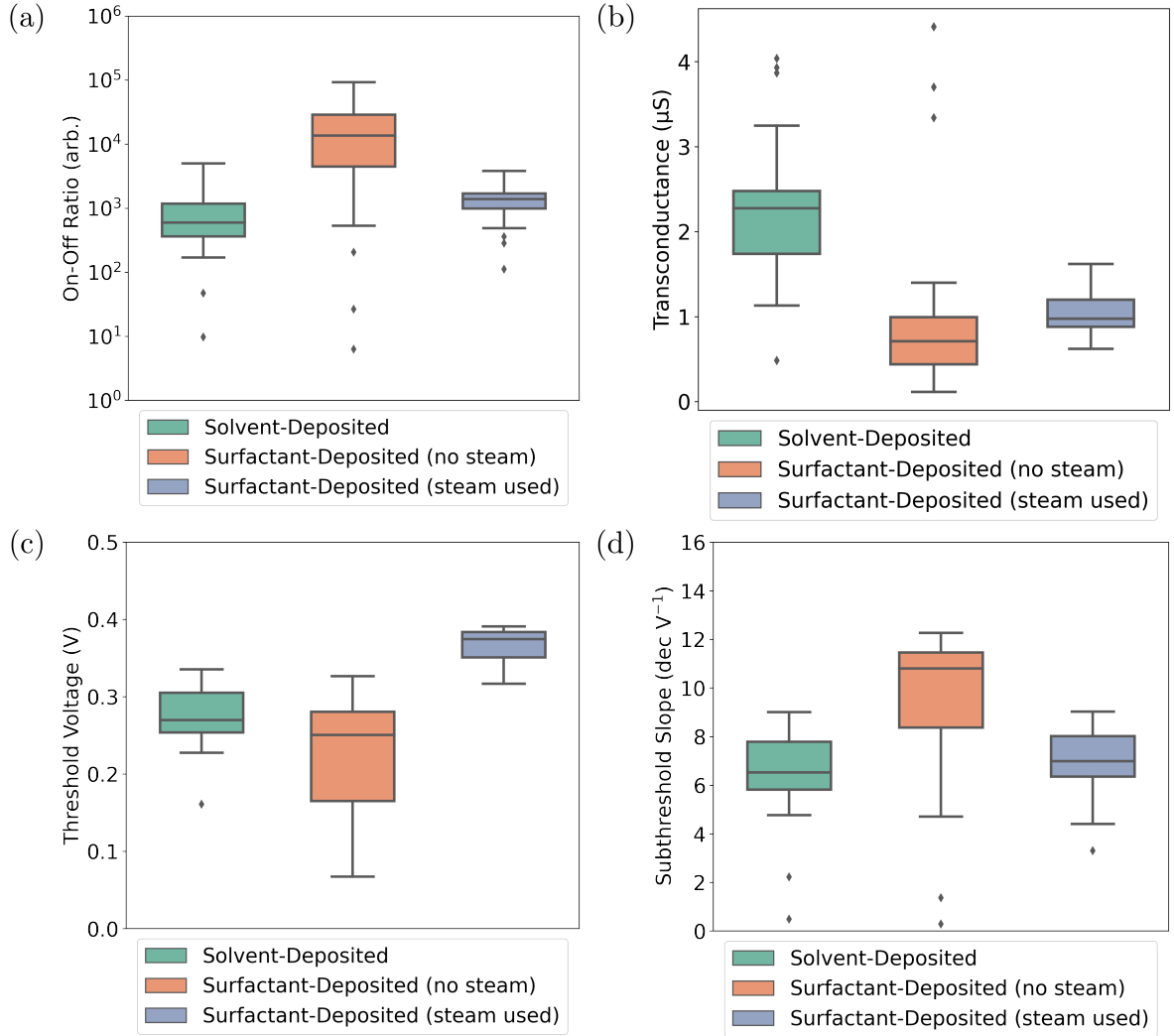


Figure 11: These boxplots illustrate the statistical distribution of (a) the on-off ratio, (b) the transconductance at $V_g = 0$ V, (c) the threshold voltage and (d) the subthreshold slope of liquid-gated and AZ® 1518 encapsulated transistor channels fabricated using solvent-deposited, surfactant-deposited or steam-assisted surfactant-deposited methods. For each deposition type, electrical characteristics were taken of 21 channels of at least three separate devices. The boxes indicate the 25th and 75th percentile of the distribution.

crease in current leakage to the backgate for larger applied voltages, despite the PBS having no visible physical contact with the Si backgate or Cu plane. This leakage current may simply be due to an increase in relative humidity around the device [@Conseil2014].

The liquid-gated devices in Figure 9 (b), Figure 9 (d) and Figure 9 (f) each exhibited ambipolar characteristics, commonly observed in liquid-gated carbon nanotube network FETs [@Kauffman2008; @Heller2009; @JongYu2009; @Derenenskyi2014; @Murugathas2018; @Albarghouthi2022]. When devices were appropriately configured, leakage current (shown by the dashed traces) did not exceed $\sim 1 \times 10^{-7}$ V across the forward and reverse sweeps. The devices shown which used steam-deposited carbon nanotube films consistently showed the least hysteresis. Section demonstrates that the mean diameter of the bundles in these films is ~ 5 nm less than those in films deposited in solvent. Hysteresis is known to scale roughly linearly with bundle diameter, due to trapped charge increasing as bundle density of states is increased [@Pop2009]. Steam-deposited devices also showed significantly less channel-to-channel variation in electrical characteristics more generally. Channel 1 in Figure 9 (b) has a much higher off-current than the other channels of the same device, which appears to be due to a unusually high proportion of metallic carbon nanotubes present in the network conduction pathways of this channel [@Rouhi2011; @Zaumseil2015].

A summary of key parameters of pristine liquid-gated devices is shown in Figure 11. The full dataset consists of three sets of 21 liquid-gated transfer characteristics of working channels, with each set corresponding to the use of a particular method of carbon nanotube network deposition in the device fabrication. Measurements from at least three devices are included in each set. Each entry in the summary corresponds to the average of the specific parameter in the forward and reverse sweep direction. When steam was used for surfactant deposition of films, the resulting devices showed highly consistent channel-to-channel electrical properties. Since the carbon nanotube films on these devices are relatively dense, as seen in Table 2, the network should be well above the percolation threshold. As many carbon nanotube pathways connect across the channel in parallel, small variations in the network morphology have less of an impact on the overall channel behaviour [@Murugathas2018]. Figure 4 and Table 2 indicate that the range of bundle sizes is relatively low in the steam-deposited films used in these devices, meaning the electrical behaviour of dominant conduction pathways is more spatially consistent. The highly consistent and reproducible subthreshold regime behaviour between channels seen for steam-deposited devices is a desirable attribute for reliable real-time multiplexed biosensing [@Kauffman2008; @Heller2009; @Gao2010].

Channels from surfactant-deposited film devices usually showed a larger on-off ratio and sub-threshold slope than those from solvent-deposited devices. Increasing the ratio of gate-sensitive semiconducting carbon nanotubes to metallic nanotubes tends to increase the on-off ratio [@LeMieux2008; @Rouhi2011; @Zaumseil2015; @Murugathas2018]. Increasing network density is expected to increase the proportion of metallic nanotubes present [@Rouhi2011], and Section indicates there are more metallic nanotubes present in the surfactant-deposited films than in the solvent-deposited films. However, percolating conduction pathways dominate device behaviour, and nanotube pathways across the channel with a lower degree of bundling

are less likely to contain metallic tubes [Murugathas2018]. Therefore, the larger on-off ratio for surfactant-deposited film devices is likely a result of their reduced nanotube bundle size and reduced bundle size variation relative to solvent-deposited films, as discussed in Section . The increased on-off ratio also results in a larger subthreshold slope, due to the lowering of off-current across orders of magnitude. A large on-off ratio and subthreshold slope both indicate reduced device power consumption. The relatively large on-off ratio and subthreshold slope of steam-deposited devices are therefore desirable for improved sensor performance [Kauffman2008; Heller2009; Gao2010].

All channels characterised had a positive threshold voltage (V_t). The threshold voltage was largest and most consistent for steam-assisted surfactant-deposited films. The steam-assisted surfactant-deposited devices had an average threshold voltage of 0.37 V, significantly higher than the to solvent-deposited and surfactant-only network devices, with average threshold voltages of 0.27 V and 0.22 V respectively. This increased threshold voltage corresponds to increased *p*-doping of the network [Kang2005; Heller2008; Murugathas2018]. As seen from Figure 2 (e)-(f) and Figure 6 (c), the steam deposition process leads to the presence of *p*-dopant contamination due to trapped water vapour or surfactant on the carbon nanotubes. It has been previously established that residual surfactant can also enhance the *p*-doping from adsorbed oxygen and water [Kane2014; Nonoguchi2018; Christensen2022]. The analysis by Kane *et al.* shows that the thermal annealing used in this work is likely inadequate for removing residual surfactant. Thermal oxidation of devices may be required for effective desorption of the persistent surfactant, as discussed in ?@sec-future-work-fabrication. Devices using films made with the other CNT deposition techniques have the advantage of not requiring careful treatment to remove surfactant.

The solvent-deposited devices had a slightly larger transconductance at $V_g = 0$ V, the operating voltage used for sensing. As the carbon nanotube networks of surfactant-deposited devices are typically much denser than solvent-deposited (Table 2), they should exhibit increased ballistic transport of charge carriers, increased mobility and therefore increased transconductance [Rouhi2011]. The observation of slightly reduced transconductance in surfactant-deposited devices ($\sim 1 \mu\text{S}$) relative to solvent-deposited devices ($> 2 \mu\text{S}$) in Figure 11 (b) is therefore surprising. However, the transconductance behaviour at $V_g = 0$ V corresponding to each device morphology partly depends on the threshold voltage. The threshold voltage determines the relative position of the transfer curve, which therefore affects the voltage corresponding to maximum transconductance. If $V_g = 0$ V is close to the point of maximum transconductance for solvent-deposited devices, slight shifts in threshold voltage may dramatically lower transconductance at $V_g = 0$ V. Surfactant deposited devices deposited without steam had a lower threshold voltage on average than the solvent-deposited devices, while the steam-assisted surfactant-deposited devices had a higher threshold voltage on average. As a larger transconductance is desirable for enhanced sensitivity and low power operation, restoring the threshold voltage by removing surfactant may be important for device optimisation.

Aqueous Sensing of Phosphate Buffered Saline Concentration

Control Series and Baseline Drift

To verify the sensitivity of the fabricated field-effect transistors and therefore test their suitability for sensing, control measurements replicating a typical sensing experiment were taken before functionalising the channels of a carbon nanotube network device. The first step to verifying device suitability was ensuring the device showed no response to $1\times$ PBS, unwanted behaviour which has previously been observed during sensing runs using similar devices [@Cassie2023]. This sequence is referred to in this thesis as the “PBS control series”. The PDMS well contained $80\ \mu\text{L}$ $1\times$ PBS at 0 s. The PBS control series ran over the first 1800 s, with $20\ \mu\text{L}$ $1\times$ PBS additions at 100 s, 200 s and 300 s, and $20\ \mu\text{L}$ subtractions at 400 s, 500 s and 600 s. The device was left untouched over the next 1200 s to allow the current level to settle, seen to be sufficient for similar devices [@Cassie2023]. The gate voltage was held at $V_g = 0\ \text{V}$.

Figure 12 (a) shows the PBS control series corresponding to each device channel alongside gate current. In both series, there is no clear stepwise response to any addition or subtraction of $1\times$ PBS. Gate leakage current remains negligible across the entire control series, with no change in response to $1\times$ PBS additions. The current has a period of short-term decay followed by much longer term baseline drift, similar to observations by Lin *et al.* and more recently Noyce *et al.* for parallel arrangements of single carbon nanotubes in air or vacuum [@Lin2006; @Noyce2019]. This effect results from hysteretic changes in the occupancy of charge traps in and around the substrate and carbon nanotubes. The magnitude of baseline drift is lower for our devices than for those characterised by Noyce *et al.*, which may be a result of numerous device and setup differences which affect the presence of charge traps. These differences include the use of liquid-gating instead of back-gating, a network of carbon nanotubes instead of single nanotubes, a different channel length, a 300 nm instead of 90 nm SiO_2 layer, a gate voltage of 0.0 V instead of -15.0 V, and an asymmetric, liquid-gated transfer sweep over a shorter voltage range when characterising devices before each control series [@Noyce2019].

Table 4: The coefficients of linear fits to the PBS control series of each channel between 1200 – 1800 s, where c_1 is the gradient and c_2 is the constant term.

Channels	CH1	CH2	CH3	CH5	CH6	CH7
$c_1\ (\text{pA/s})$	-5.1 ± 0.2	-7.2 ± 0.1	-6.5 ± 0.1	-5.0 ± 0.1	-7.6 ± 0.1	-5.1 ± 0.2
$c_2\ (\mu\text{A})$	0.316	0.316	0.308	0.218	0.364	0.332

As a first-order approximation to the longer time constant exponentials discussed by Noyce *et al.* [@Noyce2019], linear fits were performed on each PBS control series from 1200 – 1800 s. These fits are tangent to the curve of the sum of the larger time constant exponentials, and are a close approximation to this curve when higher order terms in the series expansion are

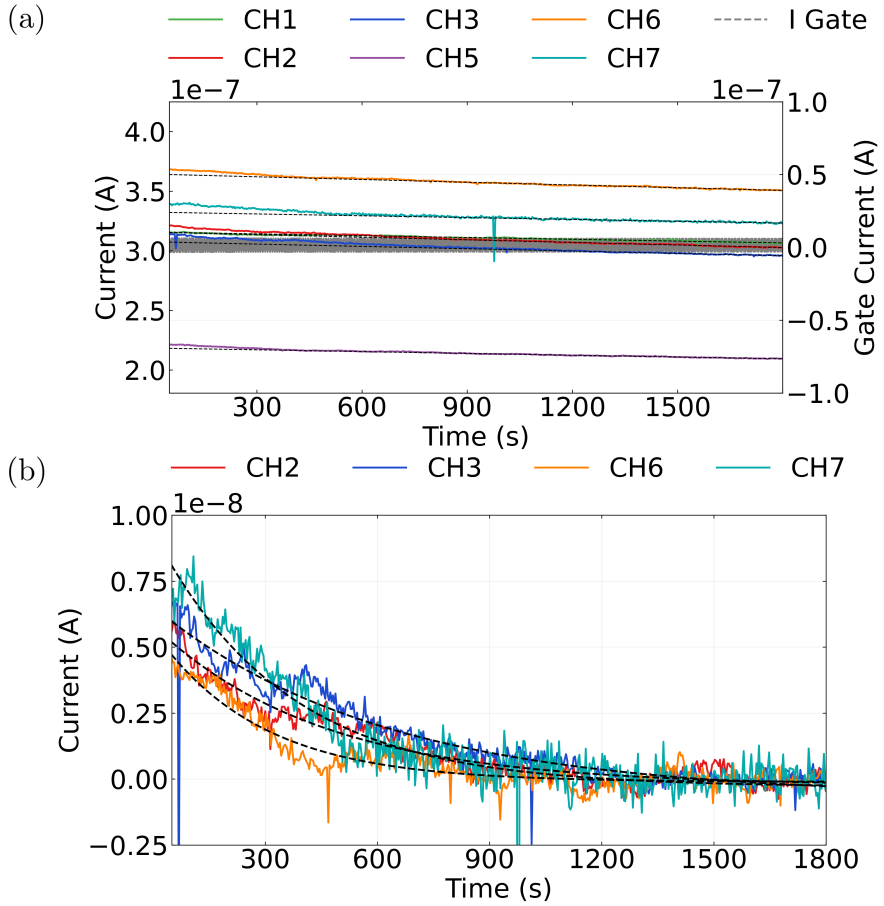


Figure 12: The transfer characteristics in (a) were taken of the steam-deposited carbon nanotube field-effect transistor used here for an example of salt concentration sensing. The absolute values of measurements are shown, so that negative values resulting from measurement error can be visualised. Linear fits to the PBS control series from each channel from 1200 s onwards are shown in (b), while exponential fits to the PBS control series from 0 – 1200 s with the linear fit subtracted are shown in (c). No significant response to PBS additions are seen at any of the addition times from 100 – 600 s.

approximately zero. This is only the case when $t \ll \tau_i$, where the time interval of interest t is much shorter than the time constants of the larger time constant exponentials, τ_i . These linear fits are shown by the dashed yellow lines in Figure 12 (a). The parameters from each fit in Figure 12 (a) are shown in Table 4, where $I = c_1 t + c_2$. Intriguingly, the fits for channels 1, 5 and 7 are all in parallel within error. Furthermore, the gradient value for each fit in Figure 12 (a) is consistent within a 2.6 pA/s range across all channels. The current data from channel 1 is closely approximated by the linear trendline across the entire control series. No short-term decay is present for this channel, indicating the channel has low net trapped charge. It is unclear why trapped charge is significantly lower for channel 1 than across the rest of the device.

Table 5: The coefficients of exponential fits to the PBS control series of each channel between 0 – 1200 s, after the linear fit has been subtracted, where I_0 is the gradient and τ is the time constant.

Channels	CH2	CH3	CH6	CH7
I_0 (nA)	6.07 ± 0.08	7.19 ± 0.11	5.75 ± 0.12	9.68 ± 0.41
τ (s)	450 ± 10	610 ± 30	280 ± 10	350 ± 30

The long-term linear fits were next subtracted from the raw control series data. Figure 12 (b) shows exponential fits to the remaining curve from 0 – 1800 s, which was successful for all channels except channels 1 and 5. The parameters from each fit are shown in Table 5, where $I = I_0 \exp(-t/\tau)$. Any constant term I_C resulting from the fit was negligible and so could be neglected. The exponential fits had characteristic time constants τ ranging between 280 – 610 s. Note that the value of peak-to-peak noise is above 5% of the initial current value for all channels. This result indicates that 3 time constants is a sufficient length of time for this short-term baseline drift to decay almost completely for each channels. At most, 1830 ± 150 s is required to minimise the drift present when sensing is performed, which is fulfilled by the chosen length of the control series.

From this analysis it appears that the baseline drift for the liquid-gated carbon nanotube devices can generally be approximated as a combination of a linear and exponential term. The exponential term corresponds to short-term, fast decaying baseline drift, while the linear term is an approximation to longer-term, slow decaying exponential baseline drift. The lack of response at all of the six PBS addition and removal times gives us confidence that this is a stable baseline which can be used for reliable sensing. Furthermore, the baseline drift can reasonably be approximated as linear after ~ 1800 s. This linear drift has a small gradient of less than -10 pA/s. The relatively small size of this drift makes it easier to distinguish responses due to analyte addition from baseline drift. It can therefore be concluded that the 1800 s length of the PBS control series is appropriate for further experimental work.

Sensing Series

A salt concentration sensing series was performed from 1800 s onwards, directly after the PBS control series. The responses to successive dilutions of the PBS gate were recorded to confirm the fabricated devices were sensitive to small environmental changes in their pristine state, to check for spurious signals, and to ensure gate current leakage or other confounding factors were not contributing to sensing responses. The PDMS well contained 80 μL 1 \times PBS at 1800 s. During the series, successive additions of deionised water were made to reduce the concentration of PBS in the well. An initial 1 \times PBS addition was performed at 2100s, to confirm no changes occurred during the PBS control series that would interfere with sensing. All additions to the well in the sensing series and resulting changes to the PBS concentration in the well are shown in Table 6.

Table 6: This table shows the times at which 20 μL additions were made to the PDMS well, with 300 s between each addition. The concentration in the well after each addition and the change in concentration after each addition are also shown. The well contained 80 μL of 1 \times PBS at 1800 s. The major component in PBS is NaCl, which has a concentration of 137 mM in 1 \times .

Addition #	1X PBS		DI Water Additions			
	1	2	3	4	5	6
Time (s)	2100	2400	2700	3000	3300	3600
Final PBS volume (μL)	100	120	140	160	180	200
Final PBS concentration	1X	0.83X	0.71X	0.63X	0.56X	0.50X
Δ PBS concentration	0	-0.17X	-0.12X	-0.09X	-0.07X	-0.06X

Figure 13 (a) shows a multiplexed salt concentration sensing series from the channels of a single AZ® 1518 encapsulated device, measured with the NI-PXIe. The gate voltage used was 0 V, which meant current measurements were well above the magnitude of the subthreshold device current. Gate current measurements did not exceed 10 nA at any point. At each of the deionised water addition times, the current traces for at least two out of six channels showed a sharp, transient increase in current followed by a return to an increased baseline. It is well established that changing the salt concentration of the liquid gate has an electrostatic gating effect on the carbon nanotubes or graphene, and changes the transfer characteristics of the channel. This shift in transfer characteristic leads to a real-time signal response to each addition [@Heller2009; @Heller2010; @Kireev2017].

Using the data in Table 4, the linear term approximating baseline drift ($c_1 t$) for each channel can be subtracted from the data in Figure 13 (a) to account for the downward drift. The mean current level just before 1800 s then becomes roughly constant. Next, each channel is normalised relative to their initial mean current level I_0 . Artifacts resulting from PXIE-2737

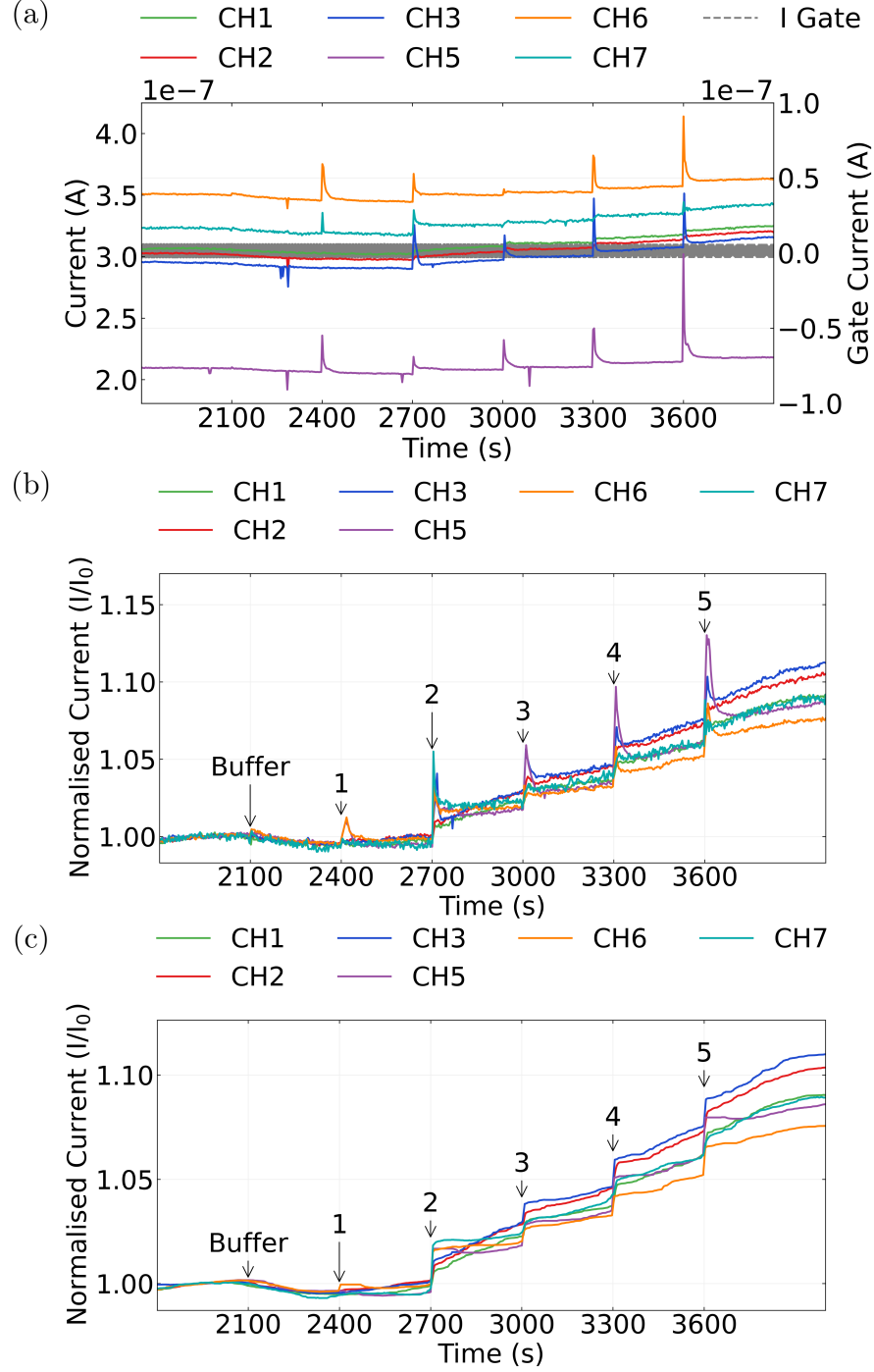


Figure 13: A multiplexed salt concentration sensing series across eight channels of a steam-assisted surfactant-deposited carbon nanotube device. The source-drain voltage V_{ds} was 100 mV, and gate voltage V_g was 0 V. In (a), the raw current measurements for each channel are shown alongside gate current. The same measurements after despiking, removal of baseline drift and normalisation to initial current are shown in (b), (c) shows the data in (b) after being processed with a moving median filter.

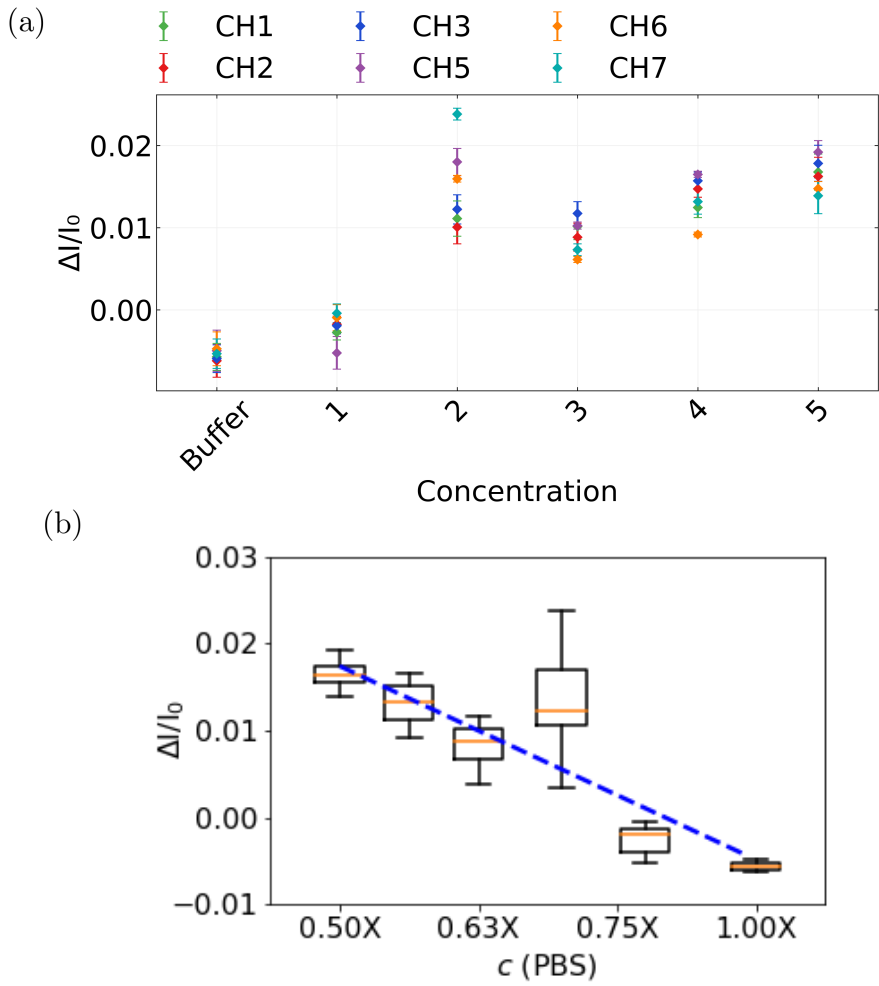


Figure 14: The signal changes in Figure 13 (c) are shown in (a). This signal data is then shown in box plot format in (b) alongside a fit to the median change in signal for each addition, where $R^2 = 0.86$.

module lag, single datapoints which fall well below the current level of the immediately preceding and succeeding datapoints, are also removed. This ‘despike’ process uses an interquartile range filter, which is described in Section . The resulting dataset is shown in Figure 13 (b). This figure shows that the signal-to-noise ratio remains roughly similar across all channels of the device. However, the behaviour of the initial transient increase with each addition is highly variable across channels and between additions for a single channel.

As measurement of the highly variable initial transient is not useful for robust sensing purposes, a moving median filter was applied, with the implementation of this filter discussed in Section . The filtered data is shown in Figure 13 (c). Noise and initial transients are removed completely, while the clearly defined step to a new current baseline is retained. Using the real-time data in Figure 13 (c), a plot of signal against addition can be created using the method described in Section , shown in Figure 14 (a). This approach illustrates the increase at each step relative to I_0 .

Intriguingly, even though the largest change in PBS concentration occurred at the first deionised water addition (see Table 6), there was very little signal change across all channels, while a relatively large change occurred at the second addition. The logarithm of final salt concentration has previously been shown to be proportional to conductance change in the linear on-regime [Heller2010]. Figure 14 (b) shows the signal change presented in terms of this logarithmic relationship. The median values of the first two additions do not line up well with the overall logarithmic trend; insufficient mixing in the tightly enclosed PDMS well environment for the first few additions may be responsible for this result. Subsequent additions may improve mixing in the well, leading to the change in concentration at the surface of the channel being more representative of the overall concentration in the well.

In Figure 13 (b) and Figure 13 (c), from around the second deionised water addition onwards, the drift behaviours of individual channels begin to significantly diverge. This deviation from the baseline drift subtracted from the raw data occurs either because the linear fit is only a first-order approximation which weakens with time, or because the additions themselves affect the drift behaviour. Displaying the data as discrete signal changes, as in Figure 14 (a), is one way of excluding these deviations (see Section). An alternative way of presenting the signal changes, by normalising relative to both I_0 and the final current reading with the formula $(I - I_0)/(I_f - I_0)$, is shown in Figure 15. This approach is useful for filtering out remaining unaccounted-for drift behaviour in order to compare the short-term transient responses to additions across the device channels. Furthermore, it lets us better understand how the short-term transient responses affect the longer-term step responses discussed earlier.

Figure 15 (a) and Figure 15 (c) show that the transient responses to DI water additions vary significantly across the surface of the device. For example, Figure 15 (c) shows that in response to the second DI water addition, channel 7 gives a large initial transient response about twice the size of the step increase between 2600 and 2800 s. Meanwhile, channels 1 and 2 show no transient response above the step increase. Figure 15 (c) indicates transient size is based on location across the device, with neighbouring channels showing the most similar behaviour. This spatially-dependent behaviour may indicate transient responses are

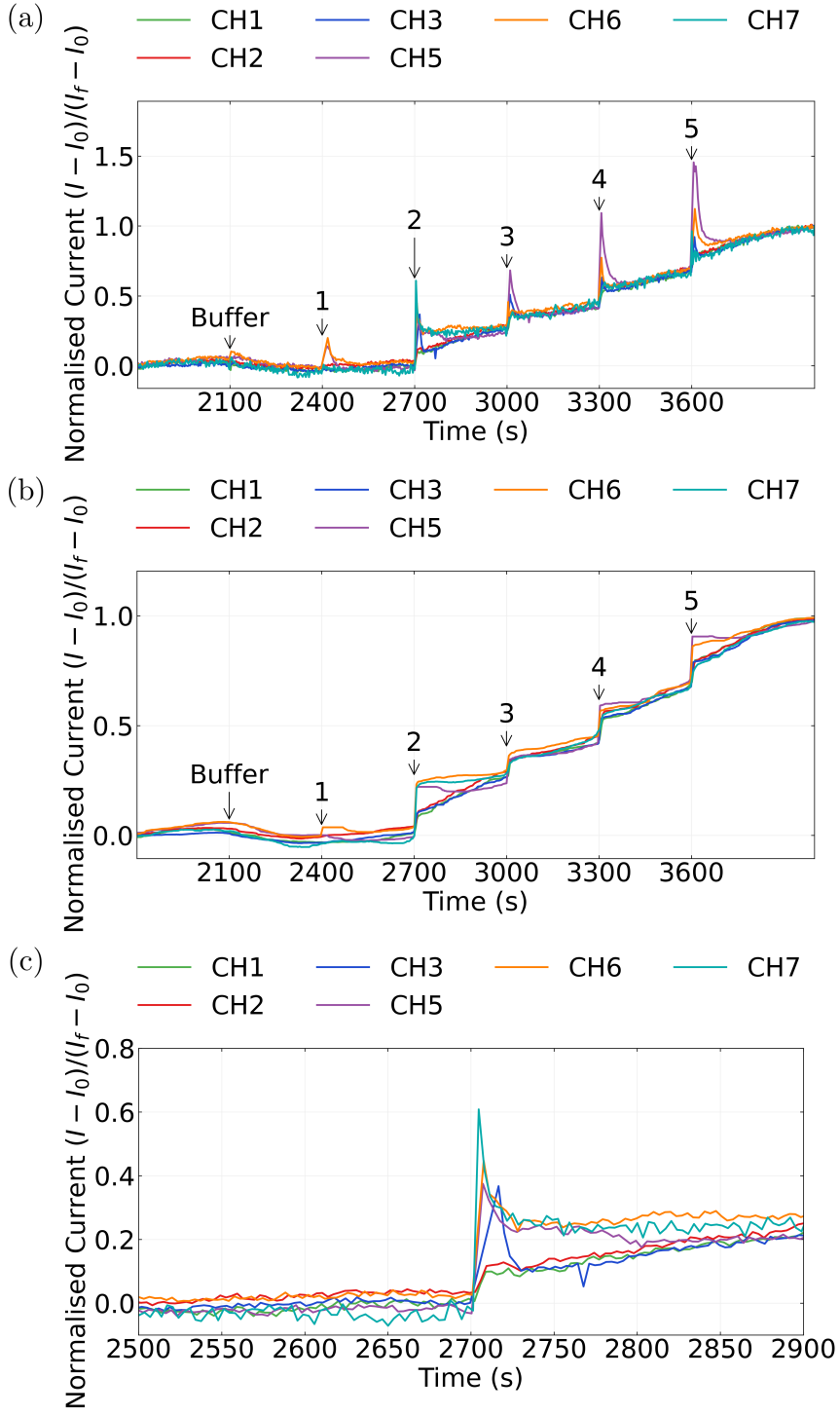


Figure 15: The processed data shown in Figure 13 (b) and Figure 13 (c) is normalised to I_0 , but an alternative normalisation can more effectively filter out remaining drift present. This normalisation presents data relative to both I_0 and the final current reading I_f using the formula $(I - I_0)/(I_f - I_0)$. Using this normalisation, the data in Figure 13 (b) and Figure 13 (c) can be displayed instead as (a) and (b) respectively. (c) shows a magnified version of the step at addition 2 in (a).

determined by the location of the channel relative to either the location of water additions or the slightly-variable location of the liquid gate. Larger and longer-lasting transient responses are not entirely removed by the moving median filter, as shown by comparing Figure 15 (a) to Figure 13 (c), and so careful placement of additions is important when sensing to minimise this effect. However, even the longest-lasting transients appear to decay to zero within about 200 s, demonstrating that a 200 s spacing between additions at minimum is necessary for reliable real-time liquid-gated sensing using this setup.

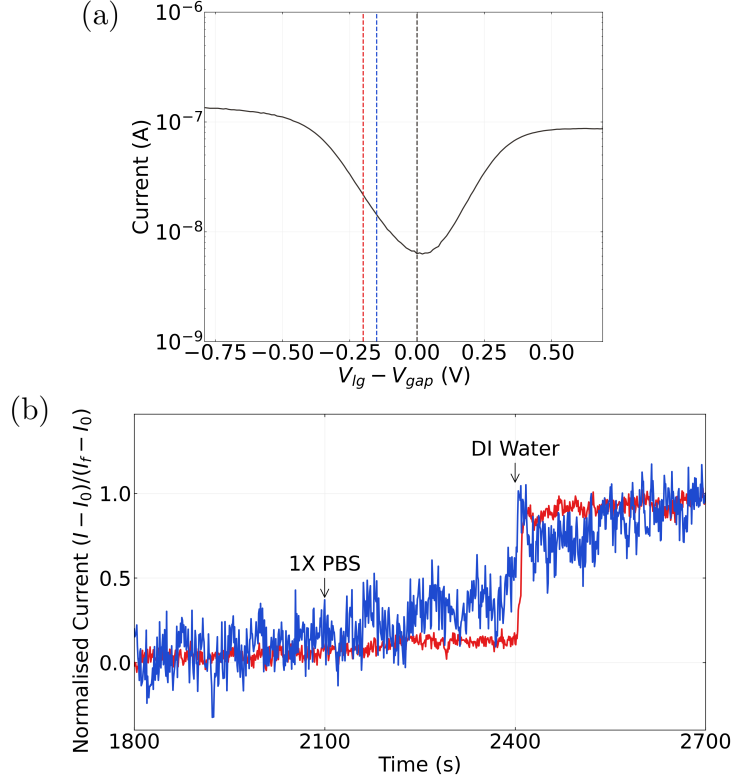


Figure 16: The transfer characteristics of a single steam-deposited carbon nanotube field-effect transistor channel are shown in (a). V_{gap} is the gate voltage corresponding to the center of the transistor bandgap, found at the minimum of the characteristic curve. The signal-to-noise ratio of the channel response to a deionised water addition after a suitable control series is shown in (b). The blue current trace in (b) was performed gating the device 150 mV away from V_{gap} , while the red current was performed gating the device 200 mV away from V_{gap} .

To explore the effect of gate voltage on signal-to-noise ratio in the subthreshold regime, two salt concentration sensing series were performed using the same channel at different gate voltages, shown in Figure 16 (a). Figure 16 (b) shows the sensing series between 1800 s and 2700 s. Previous work on the signal-to-noise ratio for liquid-gated, encapsulated carbon nanotube devices suggests that gating devices close to V_{gap} should give a larger signal-to-noise ratio for

salt concentration changes [@Heller2009]. However, in this case, a clear response to DI water was observed at a gate voltage further removed from V_{gap} , while gating with a voltage closer to V_{gap} led to a response almost indistinguishable from noise. This discrepancy could be a result of the use of a carbon nanotube network rather than a single nanotube, where gating may have less of an impact on noise. Alternatively, it could be a result of a lack of mixing in the well setup used, leading to inconsistent signal sizes across different experimental series. Heller *et al.* used a flow cell during their signal-to-ratio work [@Heller2009]. By using a flow cell with our devices, better understanding of the role of mixing in the setup used here could be achieved.

Conclusion

To ensure fabricated transistors were suitable for biosensing purposes, the morphology and electrical properties of the pristine carbon nanotube and graphene transistors were investigated.

The morphology of the carbon nanotube networks was found to have a significant impact on the electrical characteristics of the devices, determined by comparison of the skew-normal height profile of the carbon nanotube network and the key electrical parameters of a selection of carbon nanotube devices. When carbon nanotubes were deposited in solvent, the resulting networks were highly bundled ($> 97\%$ bundled) and there were large variations in bundle diameter. Liquid-gated devices created using these carbon nanotube films had highly variable on-off ratios due to the large variation in the conductive pathways available. In contrast, devices using films fabricated using surfactant with steam present showed lower bundling and less variation in bundle diameter. These films were used to create devices with improved device-to-device reproducibility of device characteristics, particularly on-off ratio. These devices also exhibited lower hysteresis, due to the relatively consistent bundle diameters and high density of these networks. When performing multiplexed sensing, consistent channel behaviour is highly desirable since comparing sensing behaviour between channels is more straightforward.

However, less bundled networks had the most surface contamination present. Atomic force microscopy indicated the presence of contamination due to steam-assisted deposition. Raman spectroscopy showed that steam deposition led to increased defects in the network, with a significantly increased D-peak to G⁺-peak height ratio. The average threshold voltage for steam-assisted surfactant-deposited network devices was significantly higher than the average threshold voltage for solvent-deposited devices, indicating these defects *p*-dope the network. The shift in threshold voltage was found to reduce device transconductance, a parameter which should be maximised for optimal sensing. Furthermore, the presence of surfactant or even trapped water could potentially have negative impacts on device functionalisation, discussed further in ?@sec-noncovalent-functionalisation. Techniques to remove contaminants may need to be explored in more detail in future works. Thermal oxidation of carbon nanotube films could be used to resolve this issue, and this is discussed further in ?@sec-future-work-fabrication.

Constant voltage real-time measurements of the carbon nanotube field-effect transistor devices had a characteristic drift that could be modelled using both a linear and exponential term. This was true for both liquid-gated and back-gated devices. The linear term of liquid-gated baseline drift had a reasonably consistent gradient between device channels, indicating that similar drift behaviour should be reproducible between devices fabricated in the same manner. The exponential behaviour was less consistent, indicating that this hysteresis behaviour is less closely correlated with the fabrication process. A control series length of 1800 s was used, as this period was sufficient to minimise exponential drift during sensing for all the channels tested. The linear and exponential terms for back-gated baseline drift under nitrogen flow were significantly higher than all measurements for liquid-gated drift. A longer control series length of 2400 s was therefore used to minimise exponential drift when vapour sensing.

A PBS dilution sensing series was used to verify that the carbon nanotube transistor devices were highly sensitive to changes in an aqueous environment. The expected logarithmic signal response behaviour was observed when detecting dilutions of PBS in a liquid-gate environment. Signal size relative to baseline drift was highly consistent between channels, which is promising for multiplexing work. Deviations from the logarithmic trend possibly indicated insufficient mixing within the PDMS well during sensing, which may be addressed in future aqueous sensing work by using a flow cell. This experiment is a useful control for sensing using functionalised devices. It is important to confirm that the devices are highly sensitive, while also being able to discern whether a signal response is due to interaction with an attached biomolecule or whether the carbon nanotubes themselves are responding.

Graphene field-effect transistor devices were often found to possess a double-minima feature, which appears to be the result of a lack of doping from the metal contacts in the center of the device channels. These double Dirac points are unlikely to have any significant effect on the sensing behaviour of graphene devices. The graphene device characteristics were found to be highly consistent after 1 hour exposure to PBS with minimal drift. There was some indications from the transfer characteristics that *p*-dopants were present on the graphene surface. Salt concentration and vapour sensing with graphene FETs are not shown in this thesis, but it is important to perform similar device verification and control testing when using a batch of graphene devices for biofunctionalised sensing.